Mechanical Engineering Faculty Research   Mechanical Engineering Department

6-2013

A Mechanism-Based Approach for Predicting Ductile Fracture of Metallic Alloys

Xiaosheng Gao
University of Akron, main campus, xgao@uakron.edu

A Mechanism-Based Approach for Predicting Ductile Fracture of Metallic Alloys

Xiaosheng Gao

Department of Mechanical Engineering, The University of Akron, Akron, OH 44325, USA
xgao@uakron.edu

Abstract   Ductile fracture in metallic alloys often follows a multi-step failure process involving void nucleation, growth and coalescence. Because of the difference in orders of magnitude between the size of the finite element needed to resolve the microscopic details and the size of the engineering structures, homogenized material models, which exhibits strain softening, are often used to simulate the crack propagation process. Various forms of porous plasticity models have been developed for this purpose. Calibration of these models requires the predicted macroscopic stress-strain response and void growth behavior of the representative material volume to match the results obtained from detailed finite element models with explicit void representation. A series of carefully designed experiments combined with finite element analyses of these specimens can also be used to calibrate the model parameters. As an example, a numerical procedure is proposed to predict ductile crack growth in thin panels of a 2024-T3 aluminum alloy. The calibrated computational model is applied to simulate crack extension in specimens having various initial crack configurations and the numerical predictions agree very well with experimental measurements.

Keywords   Ductile fracture, Unit cell analysis, Porous plasticity model, Stress triaxiality, Lode angle

1. Introduction

It is well-known that ductile fracture in metallic alloys is a process of void nucleation, growth and coalescence and this process is strongly affected by the stress state imposed on the material. Based on the fracture mechanism, a straight-forward approach to simulate ductile failure process is to model individual voids explicitly using refined finite elements [1-3]. A distinct advantage of this approach is the exact implementation of void growth behavior. It provides an effective method to study the mechanisms of ductile fracture and to analyze the trend of fracture toughness. However, due to sizeable difference between the characteristic length scales involved in the material failure process and the dimensions of the actual structural component, it is impractical to model every void in detail in structure failure analysis, especially for situations involving extensive crack propagation. For this reason, various forms of porous material models have been developed to describe void growth and the associated macroscopic softening during the fracture process. The Gurson-Tvergaard-Needleman porous plasticity model [4-6], which assumes voids are spherical in materials and remain spherical in the growth process, has been widely used in modeling ductile failure process and ductile crack extension. Gologanu, Leblond and Devaux [7, 8] extended the GTN model and derived a yield function for materials containing non-spherical voids. The GLD model can be applied to predict crack propagation in many processed materials, such as rolled plates.

In literature, the stress triaxiality ratio, defined as the ratio of the mean stress to the equivalent stress, is often used as the sole parameter to characterize the effect of the triaxial stress state on ductile fracture. However, recent studies show that the Lode parameter must be introduced to distinguish the stress states having the same triaxiality ratio [3, 9-11]. In this study, we describe a procedure to calibrate the material specific porous plasticity model so that it can accurately capture the material behavior in the fracture process zone with the influence of the stress state. A numerical approach is proposed to predict ductile crack growth in thin panels of a 2024-T3 aluminum alloy, where the GLD model is used to describe the void growth process and the material failure criterion is calibrated using experimental data. Model predictions are compared with experimental data for fracture specimens having various initial crack configurations.

2. Modeling the Material Behavior in the Fracture Process Zone

Ductile alloys used in engineering structures often contain impurities such as second-phase particles. Cavities often nucleate at relatively low stress levels due to fracture or decohesion of the large inclusions. For the purpose of analysis, voids are assumed to be present in the material at the outset of loading. These voids enlarge with increased plastic deformation and eventually coalesce with the assistance of the nucleation and growth of secondary microscopic voids. Therefore, material in the fracture process zone can be considered as an array of unit cells. Each cell is a representative material volume (RMV) containing a void nucleated from the inclusion.

2.1. Unit Cell Analysis

A straight-forward approach to study the ductile fracture mechanism as well as the effects of material properties and stress state on the material failure process is to conduct the unit cell analysis of a representative material volume (RMV). As an example, Figure 1(a) shows a 1/8-symmetric finite element model for a cubic RMV containing a spherical void and Fig. 1(b) shows the three-dimensional stress state applied on the RMV. The material is assumed to obey a power-law hardening, true stress-strain relation with Young's modulus E=70.4 GPa, Poisson's ratio v=0.3, yield stress σ_0=345 MPa and strain hardening exponent N=0.14. The initial void volume fraction (volume of the spherical void / volume of the RMV) is taken as $f_0 = 0.02$. The initial size of the RMV is defined as $X_0 \times X_0 \times X_0$ and the deformed lengths in the x-, y- and z-directions are represented by X, Y and Z respectively.
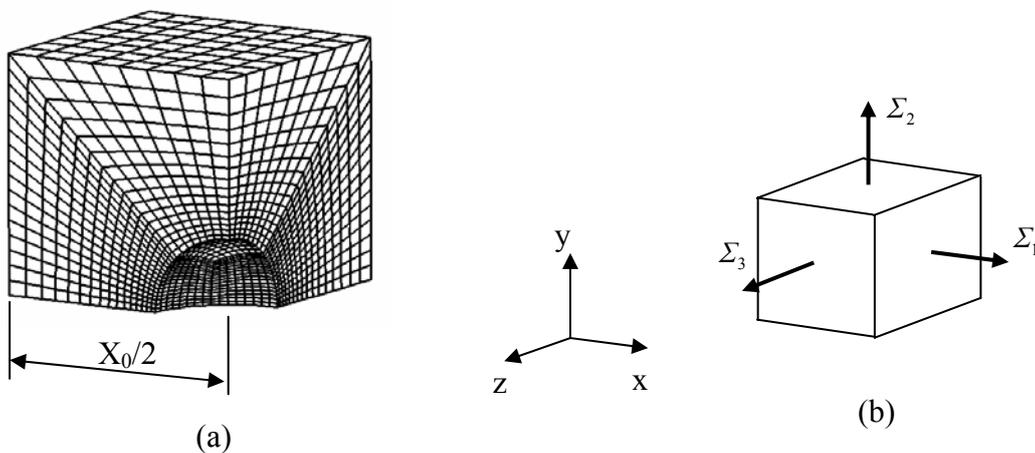

(a)

(b)

Figure 1. (a) A one-eighth symmetric finite element mesh for the RMV containing a centered, spherical void. (b) The stress state applied on the RMV.

The stress state subjected by the RMV is characterized by two parameters, the stress triaxiality ratio (T) and the Lode angle (θ)

$$T = \frac{\Sigma_1 + \Sigma_2 + \Sigma_3}{3\Sigma_e}, \quad \tan\theta = \frac{2\Sigma_3 - \Sigma_2 - \Sigma_1}{\sqrt{3}(\Sigma_2 - \Sigma_1)} \tag{1}$$

where Σ_e represents the von Mises equivalent stress. Here the numerical analyses are carried out

using the finite element program ABAQUS [12], which employs a finite strain, J_2 plasticity theory within an updated Lagrangian formulation. The displacement boundary conditions on the outer surfaces of the RMV are prescribed such that the macroscopic parameters T and θ are kept constant during the entire deformation history. Faleskog et al. [13] and Kim et al. [9] provide the details of how to prescribe the boundary conditions.

A case of axisymmetric loading is considered first, where $\Sigma_2 \geq \Sigma_1 = \Sigma_3$ ($\theta = -30^{\circ}$). Figure 2(a) shows the variation of X with the macroscopic effective strain (E_e) of the RMV. As loading continues, X gradually decreases. But when the deformation reaches a certain level, X stops decreasing and remains at a constant value. This implies that further deformation takes place in a uniaxial straining mode, which corresponds to flow localization in the ligament between adjacent voids. The shift to a macroscopic uniaxial strain state indicates the onset of void coalescence. Detailed explanation of the uniaxial straining mode can be found in references Koplik and Needleman [14] and Kim et al. [9]. Here we use E_c to denote the macroscopic effective strain at the onset of void coalescence.
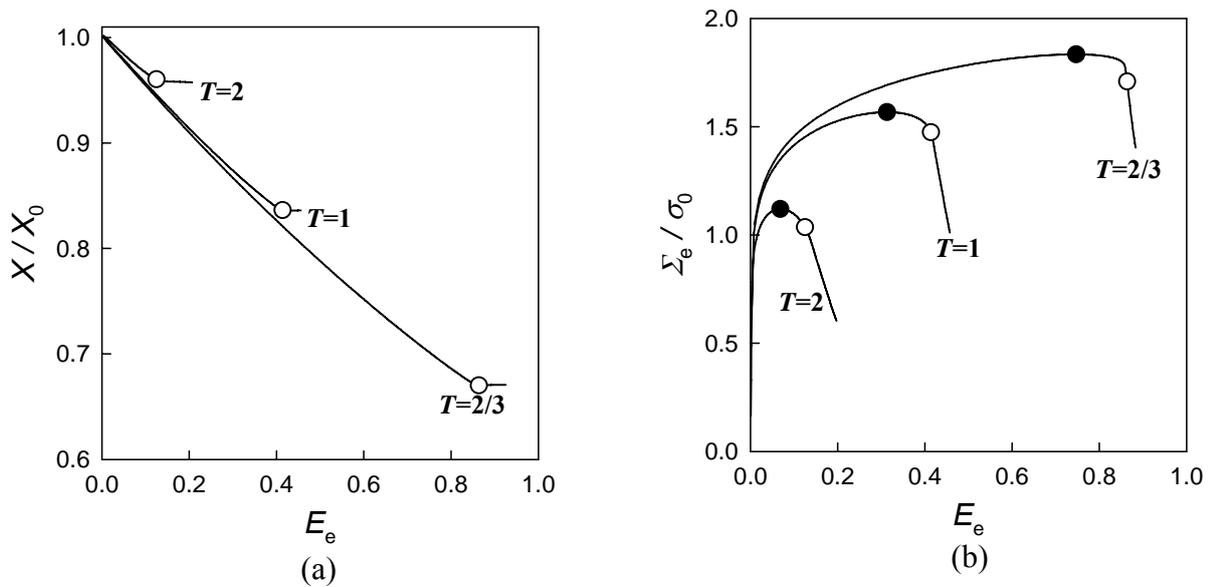

Figure 2. (a) Variation of the deformed cell width in x-direction with the macroscopic true effective strain of the cell revealing the shift to uniaxial straining. (b) Macroscopic true effective stress versus true effective strain of the void-containing RMV displaying the macroscopic softening.

The macroscopic effective stress versus effective strain curve, Figure 2(b), provides an overview of the competition between matrix material strain hardening and porosity induced softening. As deformation progresses, a maximum effective stress is reached (indicated by the filled circle), and then Σ_e decreases as strain-hardening of matrix material is insufficient to compensate for the reduction in ligament area caused by void growth. As the macroscopic effective strain reaches E_c (indicated by the open circle), a rapid drop in macroscopic effective stress occurs. As expected, both the peak stress value and the value of E_c decrease with the stress triaxiality ratio T, reflecting the decease of ductility.

In the later stage of the material failure process, secondary voids often nucleate in the ligament between enlarged primary voids and rapid growth and coalescence of these secondary voids accelerates the final ligament separation. In our analyses, it is assumed that void nucleation is plastic strain controlled and follows a normal distribution proposed by Chu and Needleman [15]. The nucleated voids are regarded to be smeared in the material and the material behavior is governed by the GTN model. Figure 3(a) compares the macroscopic effective stress versus effective strain curves between models including and not including the secondary voids. Here several values of stress triaxiality ratio, T = 1/3, 2/3, 1, 1.5 and 2, are considered. The open circles denote the onset of coalescence for models where secondary voids are not taken into account. The filled circles represent the onset of coalescence for models where nucleation, growth and coalescence of secondary voids are accounted for. It is clear that secondary voids significantly accelerate the void coalescence process.

To demonstrate the Lode angle effect on ductile failure, let the stress triaxiality ratio T be fixed and consider a series of stress states corresponding to different θ-values. Figure 3(b) shows the variation of E_c with θ as T taking a fixed value of 2/3. Clearly the Lode angle has an important effect on E_c.
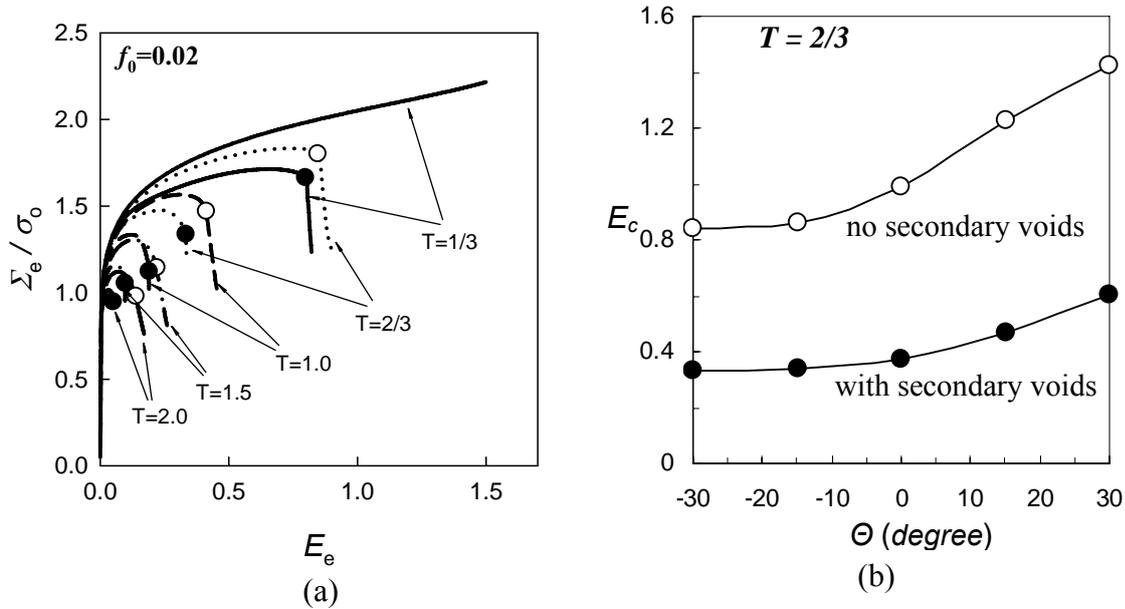

(a)

(b)

Figure 3.   (a) Comparison of the macroscopic effective stress versus effective strain curves between models including and not including secondary voids. The parameters for nucleation of secondary voids are f_N = 0.04, ε_N = 0.1 and s_N = 0.05 [15]. (b) Variation of E_c with θ as T taking a fixed value of 2/3.

Now consider an array of T and θ values and perform unit cell analysis for each case. The variation of E_c with T and θ can be expressed by a function $E_c(T,\theta)$. Therefore, a ductile failure criterion for a given material can be established as

$$E_e = E_c(T,\theta) \tag{2}$$

where E_e denote the macroscopic effective strain of the RMV. The RMV fails when E_e reaches a critical value dependent of its stress state characterized by T and θ.

Using explicit void representation, the void growth and coalescence mechanisms and the effects of the initial relative void spacing, void pattern, void shape and void volume fraction on ductile fracture toughness can also be studied directly [16].

2.2. Porous Plasticity Models

Various forms of porous plasticity models have been developed to describe void growth in ductile solids and the associated macroscopic softening, among which the most famous model is due to Gurson [4] with the modification by Tvergaard and Needleman [5, 6]. The yield function of the GTN model has the form

$$\Phi = \frac{\Sigma_e^2}{\bar{\sigma}^2} + 2q_1 f \cosh\left(q_2 \frac{3\Sigma_h}{2\bar{\sigma}}\right) - 1 - q_1^2 f^2 = 0 \tag{3}$$

where Σ_e denotes the macroscopic Mises effective stress, Σ_h represents the macroscopic hydrostatic stress, $\bar{\sigma}$ is the current flow stress of the matrix material, and f defines the current void volume fraction. The evolution law for void volume fraction is determined by requiring the matrix material to be plastically incompressible

$$\dot{f} = (1 - f)\dot{E}_{kk}^p \tag{4}$$

where $\dot{E}_{kk}^p$ is the trace of the macroscopic plastic strain rate tensor.

The GTN model was derived for growth of spherical voids, but voids are often non-spherical in actual materials. The GLD model [7, 8], with the yield function given by Eq. (5), was derived to describe the macroscopic plastic response of ductile solids containing spheroidal voids

$$\Phi = \frac{C}{\bar{\sigma}^2}\left\|\Sigma' + \eta\Sigma_h \mathbf{X}\right\|^2 + 2q(g+1)(g+f)\cosh\left(\kappa\frac{\Sigma_h}{\bar{\sigma}}\right) - (g+1)^2 - q^2(g+f) = 0 \tag{5}$$

where S is the shape parameter, $\|\ \|$ denotes the von Mises norm, Σ' is the deviatoric stress tensor, Σ_h is the generalized hydrostatic stress defined by $\Sigma_h = \alpha_2(\Sigma_{xx} + \Sigma_{zz}) + (1 - \alpha_2)\Sigma_{yy}$, $\mathbf{X}$ is a tensor defined as $\mathbf{X} = (2/3)e_y \otimes e_y - (1/3)e_x \otimes e_x - (1/3)e_z \otimes e_z$, and (e_x, e_y, e_z) is an orthogonal basis with e_y parallel to the axisymmetric axis of the void, and $\otimes$ denotes tensor product. The evolution equation for f is the same as Eq. (4) and derivations of the evolution equation for S can be found in Gologanu et al. [7, 8].

In order to simulate ductile fracture process, these porous plasticity models must be calibrated such that the material behavior in the fracture process zone is accurately captured. Calibration of these models requires the predicted macroscopic stress-strain response and void growth behavior of the representative material volume to match the results obtained from detailed finite element models with explicit void representation obtained from the unit cell analysis outlined in Section 2.1. Faleskog et al. [13], Kim et al. [9] and Pardoen and Hutchinson [17] describe the procedures to

determine the heuristic parameters in the GTN and GLD models as functions of material flow properties, void parameters and the stress triaxiality.

The porous plasticity models described above governs the behavior of the RMV during the void growth process. As the macroscopic effective strain (E_e) reaches E_c, void coalescence occurs and the RMV quickly loses its stress carrying capacity. We adopt the f^* function, introduced by Tvergaard and Needleman [6], to account for the effects of rapid void coalescence at failure. After E_e reaches E_c, f is replaced by f^* in the GLD model, where

$$f^* = \begin{cases} f, & f \le f_c \\ f_c + K(f - f_c), & f > f_c \end{cases} \tag{6}$$

In Eq. (6), f_c is the void volume fraction at $E_e = E_c$, $K = (f_u - f_c)/f_c$, and f_u is the f^* value at zero stress. Since AQAQUS/Standard does not provide an element removal procedure, Eq. (6) is employed until $f^* = 0.99 f_u$, after which an exponential function is used such that f^* gradually approaches to f_u (but can never reach f_u) to improve numerical stability.

3. Simulation of Crack Growth in Thin Panels of a 2024-T3 Aluminum Alloy

Dawicke and Newman performed extensive fracture tests on thin panels of a 2024-T3 aluminum alloy, including tests of C(T), M(T), and multi-site damage (MSD) specimens [18, 19]. Figure 4 show the sketches of the fracture specimens. The test data of our interest are from LT specimens with a sheet thickness of 2.3 mm. The specimens have very stiff guide plates (coated with Teflon tape) to constrain out-of-plane (buckling) displacements. In the L orientation, the 2024-T3 sheet material used in the experiments has a yield stress of 345 MPa, Young's Modulus of 71.3 GPa, and Poisson's ratio of 0.3. Quantitative metallographic analyses were performed to determine the inclusion volume fraction, shape and average spacing. It is found that the inclusion volume fraction (f_0) is approximately 0.002, the average spacing between inclusions in the LT plane is about 50 μm, and in LT specimens, the inclusions can be approximated as prolate spheroids with the aspect ratio ≈ 4.

To predict crack growth, the function $E_c(T, \theta)$ needs to be determined. The results presented in Section 2.1 suggest that E_c is not sensitive to θ when θ is in the range $-30^\circ \le \theta \le 0^\circ$. We perform finite element analyses of the fracture specimens considered in this study and find the θ-values of the representative material volumes ahead of the crack front are in the range of $-15^\circ \le \theta \le 0^\circ$. Therefore, we neglect the θ-dependence for these specimens and assume E_c has the following function form

$$E_c = \alpha e^{\beta T} \tag{7}$$

where α and β are two parameters need to be calibrated using experimental data. Two data points are needed to determine α and β. The tensile test provides one point. Figure 5(a) shows the 1/4 model for the tensile specimen and Figure 5(b) shows its experimental load-displacement curve. A sudden drop of the load-displacement curve suggests the onset of crack initiation. The stress and strain states for the critical element (at the geometry center of the specimen) at crack initiation are obtained through finite element analysis. The triaxiality T and strain ε_f are calculated as 0.45 and 0.5 respectively. Substitution of these values into Eq. (7) yields a relationship between α and β, $0.45 = \alpha e^{0.5\beta}$. The next step of the calibration process seeks to match the model predicted load versus crack propagation curve with the experimental measurements for the C(T) specimen. This step entails several finite element crack growth analyses of the C(T) specimen using different values of β.
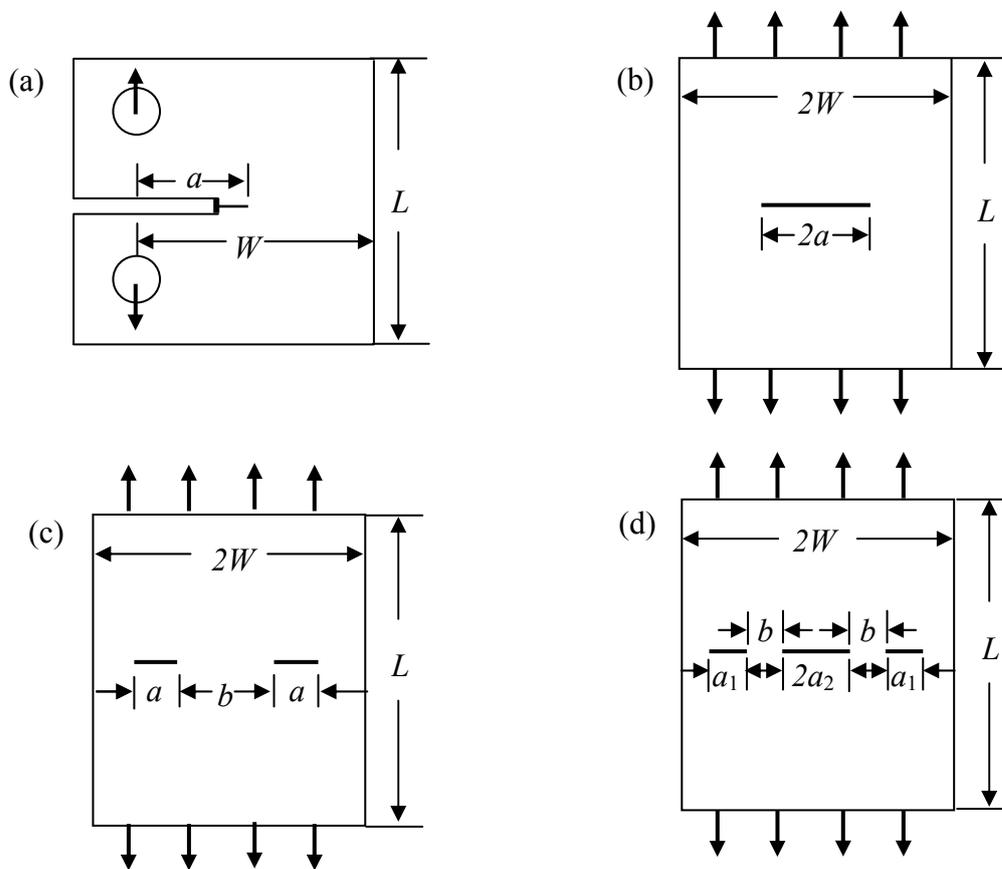

Figure 4. Fracture specimens: (a) C(T) specimen, (b) M(T) specimen, (c) MSD specimen containing two cracks, (d) MSD specimen containing three cracks.

The C(T) specimen has a width of 150 mm with $a/W = 0.33$, where a represents the initial crack length and W represents the specimen width. The quarter-symmetric finite element mesh has 27,400 eight-node, isoparametric solid elements (with reduced integration). The mesh near the crack front has six layers with varying thickness to capture the stress gradient in the thickness direction, where the thickest elements are at the symmetry plane. The elements directly ahead of the crack front have uniform in-plane dimensions ($L_e = 50$ μm) and are governed by the GLD model. All other elements follow J_2 flow plasticity. Loading of the C(T) specimen is controlled by prescribing a displacement
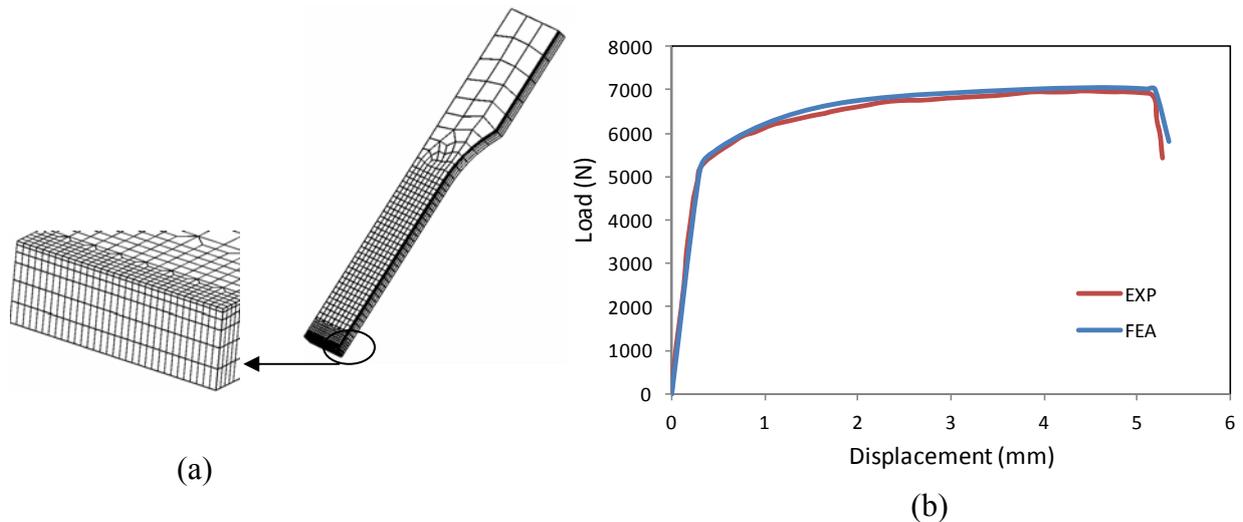
on a rigid pin through the hole.

(a)

(b)

Figure 5. (a) Finite element mesh for the tensile specimen. (b) Comparison of the predicted and experimental load-displacement curves.

Figure 6 shows the comparison between the model predicted load versus crack growth curve with the experimental measurements (two sets of experimental data) for different choices of α and β, where the lines represent model predictions and the symbols denote experimental measurements. Here Δa represent the amount of crack growth measured at the free surface. In the numerical model, the propagating crack front is defined by the elements which have reached the failure strain E_c. From Figure 6, it can be seen that the choice of $\alpha = 0.93$ and $\beta = -1.45$ (solid line) results in a best fit to the experimental data. Therefore, these values are the calibrated values for α and β and will be used to predict crack growth in other fracture specimens.
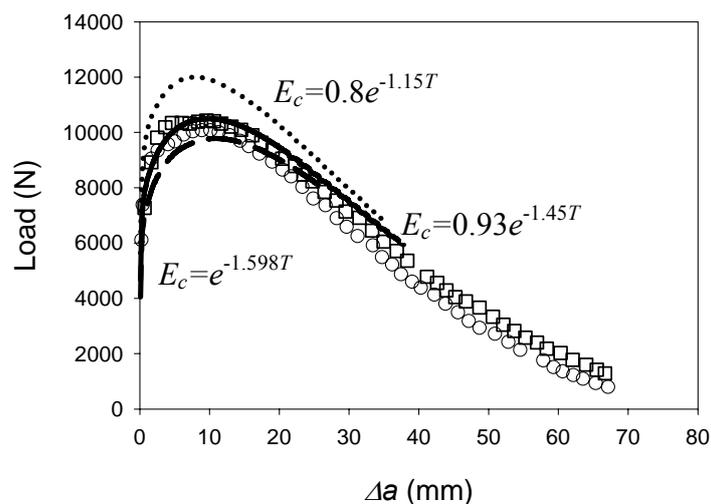

Figure 6. Comparison of the model predicted load versus crack growth curve with the experimental measured data (symbols) showing the choice of $\alpha = 0.93$ and $\beta = -1.45$ (solid line) results in a best fit to the experimental data.

The calibrated computational model is now employed to predict the crack extension behavior of M(T) and MSD specimens. Three M(T) specimens with $W = 300$ mm and a/W ratios of 0.33, 0.42 and 0.5 are analyzed. The element size and arrangement in the region near the crack front are kept the same as used in the C(T) specimen. The nominal remote stress, σ_R, characterizes the loading for these specimens. Figure 7(a) compares the computed load versus crack extension responses with experimental measurements, showing very good agreement for all three cases. Figure 7(b) compares the computed load versus crack extension responses with experimental measurements for a MSD specimen containing three cracks as shown in Figure 4(d). This specimen has the same width as the M(T) specimens. The center-crack length is $2a_2 = 100$ mm. The two lead cracks have the same length of $a_1 = 12.5$ mm. The tip-to-tip distance between the lead crack and the center crack is $b = 12.5$ mm. The model prediction captures accurately the load versus crack extension curve. The cusp on the predicted load versus crack extension curve corresponds to the point when the lead crack and the center crack link up.
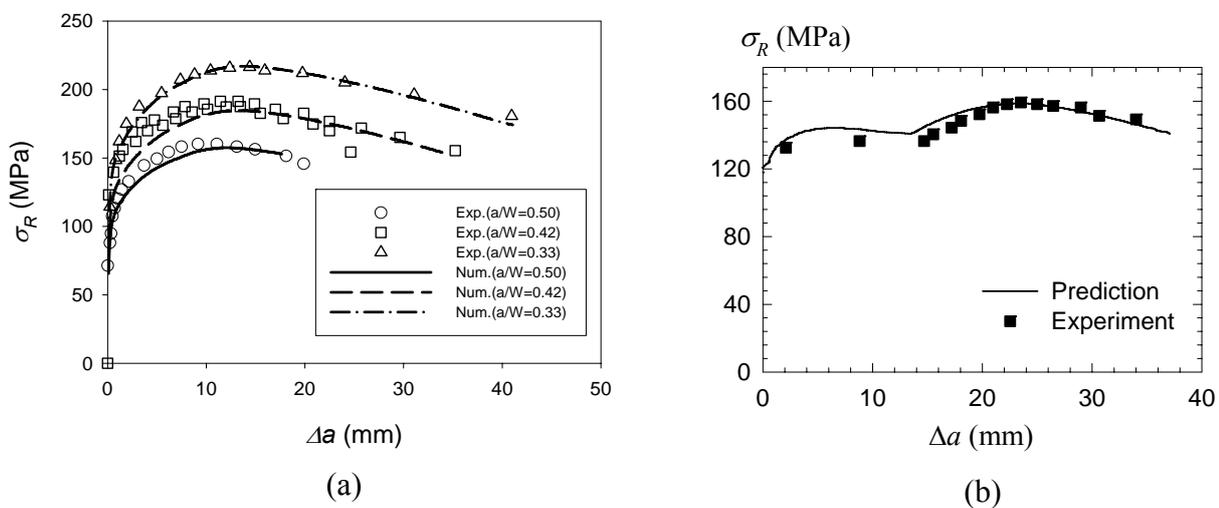

Figure 7. Comparison of the model predicted load versus crack extension responses (lines) with experimental measurements (symbols): (a) M(T) specimens, (b) MSD specimen containing three cracks.

4. Concluding Remarks

Based on the mechanism of ductile fracture in metallic alloys, this paper describes a method to predict crack growth in engineering structures. To model extensive crack extension, homogenized porous plasticity models need to be adopted to describe the material behavior in the fracture process zone and these models must be calibrated such that the material behavior is accurately captured. Unit cell analysis of the representative material volume reveals the strong effect of the stress state on the void growth and coalescence. Calibration of the porous plasticity models requires the predicted macroscopic stress-strain response and void growth behavior of the representative material volume to match the results obtained from detailed unit cell analysis. As an application, a numerical procedure is proposed to predict ductile crack growth in thin panels of a 2024-T3 aluminum alloy. The material specific GLD porous plasticity model is used to describe the void growth process and the failure criterion is calibrated using experimental data. The calibrated computational model is then applied to predict crack extension in fracture specimens having various initial crack configurations. The numerical predictions show good agreement with experimental

measurements.

References

[1] V. Tvergaard, J.W. Hutchinson, Two mechanisms of ductile fracture: void by void growth versus multiple void interaction. Int J Solids Struct 39 (2002) 3581-3597.

[2] J. Kim, X. Gao, T.S. Srivatsan, Modeling of crack growth in ductile solids: a three-dimensional analysis. Int J Solids Struct 40(2003) 7357-7374.

[3] J. Kim, G. Zhang, X. Gao, Modeling of ductile fracture: application of the mechanism-based concepts. Int J Solids Struct 44 (2007) 1844–62.

[4] A.L. Gurson, Continuum of ductile rupture by void nucleation and growth: Part I-Yield criteria and flow rules for porous ductile media. J Eng Mater Tech 99(1977) 2-55.

[5] V. Tvergaard, On Localization in ductile materials containing spherical voids. Int J Fract 18(1982) 237-252.

[6] V. Tvergaard, A. Needleman, Analysis of the cup-cone fracture in a round tensile bar. Acta Metall 32(1984) 157-169.

[7] M. Gologanu, J.B. Leblond, J. Devaux, Approximate models for ductile metals containing nonspherical voids – Case of axisymmetric prolate ellipsoidal cavities. J Mech Phys Solids 41(1993) 1723-1754.

[8] M. Gologanu, J.B. Leblond, J. Devaux, J., Approximate models for ductile metals containing nonspherical voids – Case of axisymmetric oblate ellipsoidal cavities. J Eng Mater Tech 116(1994) 290-297.

[9] J. Kim, X. Gao, T.S. Srivatsan, Modeling of void growth in ductile solids: effects of stress triaxiality and initial porosity. Eng Frac Mech71(2004) 379-400.

[10] L. Xue, T. Wierzbicki, Ductile fracture initiation and propagation modeling using damage plasticity theory. Eng Fract Mech 75 (2008)3276–93.

[11] K. Nahshon, J.W. Hutchinson, Modification of the Gurson model for shear failure. Eur J Mech A/Solids 27(2008) 1-17.

[12] SIMULIA, ABAQUS User's Manual (version 6.9), Providence, RI, 2008.

[13] J. Faleskog, X. Gao, C.F. Shih, Cell model for nonlinear fracture analysis-I. Micromechanics calibration. Int J Fract 89(1998) 355-373.

[14] J. Koplik, A. Needleman, Void growth and coalescence in porous plastic solids. Int J Solids Struct 24(1988) 835-853.

[15] C. Chu, A. Needleman, Void nucleation effects in biaxially stretched sheets. J Eng Mater Technol 102(1980) 249–256.

[16] X. Gao, T. Wang, J. Kim, On ductile fracture initiation toughness: Effects of void volume fraction, void shape and void distribution. Int J Solids Struct 42(2005) 5097-5117.

[17] T. Pardoen, J.W. Hutchinson, An extended model for void growth and coalescence. J Mech Phys Solids 48(2000) 2467-2512.

[18] D.S. Dawicke, J.C. Newman, Evaluation of fracture parameters for prediction residual strength of multi-site damage cracking, in: Proceedings from the First Joint NASA/FAA/DoD Conference on Aging Aircraft, 1997, pp. 1307–1326.

[19] D.S. Dawicke, J.C. Newman, J.C., Residual strength predictions for multiple site damage cracking using a three-dimensional finite element analysis and a CTOA criterion, in: T.L. Panontin, S.D. Sheppard (Eds), Fracture Mechanics: 29th Volume. ASTM STP 1321, Philadelphia, PA, 1998, pp. 815–829.